Available online www.jocpr.com

Journal of Chemical and Pharmaceutical Research, 2016, 8(1):712-728

Research Article

ISSN : 0975-7384
CODEN(USA) : JCPRC5

Phan-Thien-Tanner modeling of a viscoelastic fluid flow around a cylinder in a duct

[*]M. Y. Abdollahzadeh Jamalabadi and M. Oveisi

Maritime University of Chabahar, Chabahar, Iran

ABSTRACT

Numerical solutions are obtained for the 2D confined plane viscoelastic flow around a confined cylinder. The Navier-Stokes momentum differential fluids, whilst for the viscoelastic case different constitutive equations are utilised.Finite element scheme is implemented to represent the convective terms in the constitutive equations for the Phan-Thien-Tanner fluids, and the resulting predictions of the drag coefficient on the cylinder are shown to be as accurate as existing numerical predictions. In this context, a Taylor-Galerkin/pressure correction finite element method has been adopted for the parabolic-elliptic momentum-continuity equations, whilst a finite volume implementation is utilised for the hyperbolic sub-system comprising of the constitutive equation..

Keywords: Social impact, economic analysis, solid oxide fuel cell, clean energy

---

INTRODUCTION

The numerical simulation of viscoelastic flows with free-surfaces is a relevant problem to the modelling of several shaping processes in the polymer industry, such as extrusion or injection moulding. Polymer melts are typical examples of viscoelastic materials. Any dissolved elastic component, be it polymers or biological molecules, will give rise to viscoelastic effects. Such effects require the use of models that take the fluid's memory of past deformations into account. Differential constitutive equations are able to do just this, and they provide a good quantitative agreement with experiments Baaijens et al. (1997). As a result, the constitutive behaviour of the material depends on its strain history [1].

This was effectively solved, when loss of positive definiteness for the conformation tensor was recognized as the cause of the singularity and the log-conformation method was introduced as a remedy Hulsen et al. (2005).

Many complex fluids of interest exhibit a combination of viscous and elastic behavior under strain. Examples of such fluids are polymer solutions and melts, oil, toothpaste, and clay, among many others. The Oldroyd-B fluid presents one of the simplest constitutive models capable of describing the viscoelastic behavior of dilute polymeric solutions under general flow conditions. Despite the apparent simplicity of the constitutive relation, the dynamics that arise in many flows are complicated enough to present a considerable challenge to numerical simulations.

In shear flows, the viscoelasticity produces a normal stress difference $\tau_{xx} - \tau_{yy}$. A typical example of a viscoelastic effect happening in the manufacturing industry is the *extrudate swelling*. Another viscoelastic effect is the *elastic turbulence* in curvilinear flows, at very low Reynolds number *Re* (below unity) [2-4]. Recently, Morozov and

Saarloos [5] summarized theoretical and experimental evidences of the existence of a *subcritical elastic instability* due to normal stress effects, in planar flows. Linear and non-linear stability analysis [6] showed that the viscoelastic Poiseuille flow is linearly stable at all Weissenberg numbers, but becomes nonlinearly unstable at a Weissenberg number around 4, where the Weissenberg number *Wi* is the dimensionless quantity accounting for the anisotropy created by the normal stress difference:

$$Wi = \left(\tau_{xx} - \tau_{xx}\right)/\tau_{xy},$$

The numerical simulation of viscoelastic flows has for a long time been very challenging, because of the so-called *high Weissenberg number problem* [7]. Numerical investigations show that the simulations are prone to *numerical instability* (divergence of the calculation) for *Wi* above the unity. Another numerical difficulty comes from the resolution of the Navier-Stokes equations at low *Re*, where classical fractional-step methods lose their efficiency. In this paper, we present a numerical framework which avoids these two difficulties with two changes of variables: the *logarithmic-conformation representation* [8,9], and the *pure-streamfunction flow formulation* [10,11], as described in the section 3. Both reformulations enhance the robustness of the simulation.

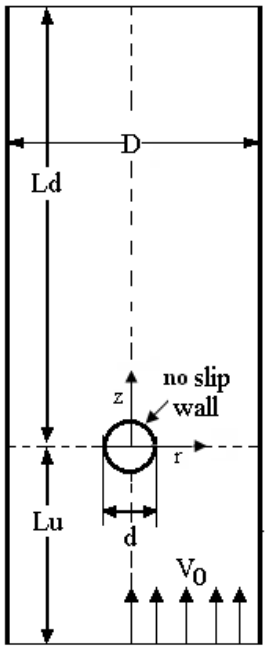

Figure 1. Schematic diagram of flow around a cylinder in a channel

When it comes to the modelling of free-surfaces, Lagrangian methods have the advantage to solve directly the position of the surface (coinciding with the position of mesh), without additional calculations, see for instance [12,13]. However, Lagrangian methods become difficult to use when the free-surfaces experience changes of topology, e.g. when surfaces split or merge. For this reason, Eulerian methods are more suitable in general cases. Thus, free-surface problems are typically solved as bi-phasic flows, where one is of the fluid phase is simply air. In the Eulerian methods, the position of the interface between the two phases is represented through the use of an additional discrete variable. We chose to use the *volume-of-fluid* (VOF) method [14-16], where the additional variable is the volume fraction of the two phases, which is transported with the flow.

The goal of this research is to model the flow of an elastic polymer and find a correlation between the first normal stress difference and the pressure drop. The normal stress difference is very difficult to measure in practice, but very important in determining the viscoelastic properties of the fluid. However, pressure is very easy to measure, and if a correlation between the two can be determined, the pressure drop could then be used to determine these viscoelastic properties, more specifically: elasticity and Weissenberg number. The same type of phenomenon was already

observed for non-Newtonian viscoelastic fluids although in this case as a consequence of more complex and less understood effects. Fellouah et al. [17] numerically and experimentally studied Dean instabilities using power-law and Bingham fluids in a curved duct of rectangular cross-section. Independently, Iemoto et al. [18] and Das [19] verified that the secondary flow of a purely viscous fluid (following a power law [18] and a Bingham [19] model) is weaker than that of a viscoelastic fluid (considering a White–Metzner model), in a curved pipe. From a similarity solution for an Oldroyd-B fluid flowing in the region between two circular concentric cylinders of large radius, with radial injection of fluid at the outer cylinder wall, Phan-Thien and Zheng [20] found that the flow kinematics was very close to that for a Newtonian fluid under the same conditions. In this problem, secondary flows were absent. More relevant to the present work, in a series of studies of flows in annular spaces with rectangular cross-section, Joo and Shaqfeh [21], [22] and [23] reported a purely elastic flow instability, which had not been studied before and was found to be stationary in pressure driven Dean flow of an Oldroyd-B fluid. In addition, they showed that this so-called purely elastic Dean flow is destabilized by inertia. For the same fluid model, Sarin [24] studied the effects of Deborah number on the position of the maximum axial velocity and of the centre of vortices, and verified an increase in the magnitude of secondary flows, in curved pipe. The effects of rotation about z-axis (normal to the flow direction axis) on secondary flow intensity, axial velocity and axial normal stress were investigated by Zahng et al. [25] for an Oldroyd-B fluid flow in a curved duct of square cross-section. They concluded that all the parameters they focused in are affected by rotation, generating multiple pairs of vortices. Recently, Norouzi et al. [26] focused on the effects of centrifugal force due to the curvature of the rectangular cross-section duct and the opposite effects of the first and second normal stress differences on the flow field, considering a second-order fluid. Their numerical results showed that while the first normal stress difference favours the transition from one to two pairs of vortices, the second normal stress difference has the opposite effect. Also considering a second-order fluid, but flowing in a curved pipe, Sharma and Prakash [27] established that the first normal stress difference intensifies the secondary flow. Also for a curved pipe, Fan et al. [28] subsequently confirmed the finding for the Oldroyd-3-constant fluid model (which includes the Upper–Convective–Maxwell and Oldroyd-B models) and showed that the negative second normal stress difference has the opposite effect, i.e., it decreases the intensity of the secondary flow. Helin et al. [29] presented results on the development of the flow in a curved duct with square cross-section considering two viscoelastic fluids, namely the Oldroyd-B model and a modified version of the Phan–Thien–Tanner (PTT) model. For the former, the magnitude and intensity of the secondary vortices increase with elasticity, and for the later the onset of the second pair of vortices in the secondary flow takes place at lower Reynolds numbers as Deborah number increases. The later result was also numerically verified by Boutabaa et al. [30], considering the same geometry [31-38].

Of the two types of sudden contraction flow geometries, the one that has received more attention, both numerically and experimentally, is the axisymmetric configuration. The planar configuration, on the other hand, is better suited to visualisation studies through birefringence strand techniques, as in the works [39], [40] and [41], and is equally relevant to engineering flows in extrusion dies. In a previous papers [42-45], we have reviewed the published numerical work on planar contraction flows and have provided numerical solutions based on the upwind scheme but using very refined meshes. Later [46], we published accurate results for the case of the flow of an upper convected Maxwell (UCM) fluid, giving special attention to issues of accuracy and mesh refinement, particularly to the effects brought about by improved numerical spatial discretisations in contrast to plain upwind differencing. Amongst the more recent computational work we emphasise that of Aboubacar and Webster [47] and Aboubacar et al. [48] who have done a very comprehensive study of Oldroyd-B and PTT fluids flowing through sharp and rounded-corner planar contractions, having highlighted the influence of the fluids Trouton ratio on the vortex patterns. Although the conclusions of these authors regarding flow behaviour in planar contractions are indisputably correct, as we shall show their data still lack the degree of accuracy required for benchmark data and that is the gap we would like to fulfil with this work.

EXPERIMENTAL SECTION

The governing equations of the viscoelastic flows consist in the continuity equation ($\rho\nabla.u = 0$ conservation of mass)

$$\nabla \cdot \boldsymbol{u} = 0,$$

and the momentum equation ($\rho(u.\nabla)u = \nabla.(-pI + \mu\left[\nabla u + (\nabla u)^T\right] + F)$ conservation of linear momentum)

$$\rho\left(\frac{\partial \boldsymbol{u}}{\partial t}+\boldsymbol{u}\cdot\nabla\boldsymbol{u}\right)=-\nabla p+\mu_{\mathrm{S}}\nabla^{2}\boldsymbol{u}+\nabla\cdot\boldsymbol{\sigma},$$

where u is the velocity vector, p is the isostatic pressure and σ the viscoelastic extra-stress tensor. The left hand side in the equation corresponds to the inertial effects; the three terms on the right hand side of equation are the contributions of the pressure gradient, the Newtonian viscous stress of the solvent, and the viscoelastic stress of the polymers, respectively. Finally, the equations of conservation are supplemented with a constitutive model which closes the system of equations [49]. We use a generic partial-differential viscoelastic model of general form

$$\frac{\partial \boldsymbol{\sigma}}{\partial t}+\boldsymbol{u}\cdot\nabla\boldsymbol{\sigma}$$
$$-\left(\boldsymbol{\sigma}\cdot\nabla\boldsymbol{u}+\nabla\boldsymbol{u}^{\mathrm{T}}\cdot\boldsymbol{\sigma}\right)+\frac{f(\boldsymbol{\sigma})}{\lambda}\boldsymbol{\sigma}=\frac{2\mu_{\mathrm{P}}}{\lambda}\dot{\boldsymbol{\varepsilon}},$$

where f (σ) is a relaxation function, and $\dot{\boldsymbol{\varepsilon}}=(\nabla\boldsymbol{u}+\nabla\boldsymbol{u}^{\mathrm{T}})/2$ is the strain rate tensor. Depending on the expression of f (σ), popular viscoelastic models can be recovered [1], see table 1. The material parameters ρ, μS, μP and λ are the density, the solvent viscosity, the polymer viscosity and the relaxation time, respectively. Table 1 defines the terms mentioned above [51-63].

ε is Elasticity of the fluid, parameter in PTT model; ΔP/L Predicted drop in pressure for fully developed flow per unit length using the Phan-Thien-Tanner (PTT) model; ΔP_{excess_1} isThe difference of the measured drop in pressure through the model and thedrop in pressure that occurs when We = 0; ΔPexcess2 is the difference of the measured drop in pressure through the model and the fully developed pressure drop in PTT; τxx Shear stress at the inlet, also the normal stress at the inlet. We: is Weissenberg Number: λ<u>/y; Where λ is the time constant that describes how fast the polymer "forgets" its shape, <u> is the average velocity, and y is half the height of the model.

In a porous medium

$$\begin{bmatrix} u \\ \tau \end{bmatrix}_y = \begin{bmatrix} f & \dfrac{\sigma}{\tau} & \dfrac{1}{\lambda(2-\xi)} \\ p_x & -au & -bu \end{bmatrix} \quad ,$$

where

$$a=\frac{\mu}{k} \quad , \quad b=\frac{pc_f}{\sqrt{k}}$$

Table 1. Expressions of the relaxation function *f* (*σ*) in the generic constitutive equation (4), for different viscoelastic models

Viscoelastic model	Relaxation function $f(\boldsymbol{\sigma})$
Oldroyd-B	1
Giesekus	$1+(\alpha\lambda/\mu_1)\boldsymbol{\sigma}$
Linear PTT	$1+(\varepsilon\lambda/\mu_1)\,\mathrm{tr}(\boldsymbol{\sigma})$
Exponential PTT	$\exp\left[(\varepsilon\lambda/\mu_1)\,\mathrm{tr}(\boldsymbol{\sigma})\right]$
FENE-CR	$\left[1+(\lambda/\mu_1 L^2)\,\mathrm{tr}(\boldsymbol{\sigma})\right]^{-1}$

In dimensionless forms:

$$\sigma_x^* = \frac{\sigma_x}{n/2\lambda} = \frac{1-\sqrt{1-\xi(2-\xi)\tau^{*2}}}{\xi}$$

and

$$\tau^* = \frac{p_x y}{n/2\lambda}$$

where $\lim_{\xi \to 0} \sigma_x^* = \tau^{*2}$

So $f = 1+\varepsilon\frac{\sigma_x^* + \sigma_y^*}{2}$ in Linear PTT and $\sigma_y = \sigma_x \frac{-\xi}{2-\xi}$. In a same way :

$$\rightarrow f = 1+\frac{1-\xi}{2-\xi}\varepsilon\sigma_x^*$$

Which has a solution of

$$u_y\Big|_{\xi=0} = \gamma = \frac{1}{\lambda(2-\xi)}\left(\tau^* + \frac{1-\xi}{2-\xi}\varepsilon\tau^{*3}\right)$$

or

$$u = \frac{p_x}{\eta}y^2 + \frac{\varepsilon\lambda^2 p_x^3}{\eta^3}y^4 + u_{\max}$$

while for this research, we non-dimensionalized every quantity; that with our boundary conditions (described in the next section) give us the following relations:

$$u = \frac{p_x}{\eta}\mathrm{Y}^2 + \frac{\tau_w}{\eta}\mathrm{Y} +$$

$$\frac{\varepsilon\lambda^2}{\eta^3}\left(p_x^3\mathrm{Y}^4 + 4p_x^2\tau_w\mathrm{Y}^3 + 6p_x\tau_w^2\mathrm{Y}^2 + 4\tau_w^3\mathrm{Y}\right)$$

is comparable to

$$u = \frac{p_x}{2\mu}y(y-h)$$

To use the correlations above, the term,ΔP must be calculated at the given ε and We.

The first normal stress difference, N, is calculated as N = τxx - τyy, but these stresses are measured at the inlet where τyy = 0, so N = τxx.

from continuity

$$V_y = -u_x \rightarrow V = -\frac{p_{xx}}{2\mu}\left(\frac{y^3}{3} - \frac{y^2 h}{2} + c\right)L$$

With BC of

$$C \rightarrow V(0) = 0$$

and from symmetry ($p_x\big|_0=0$) at BC

$$V(h)=-V_m=\frac{p_{xx}h^3}{12\mu}\rightarrow p=\frac{-6\mu V_m}{h^3}x^2+p_0 \text{ for half length}$$

$$\frac{p-p_\infty}{\mu V_m/h}=6\left(\frac{x}{h}\right)^2\xrightarrow{x=l/2}\Delta p^*_{\max}=\frac{3}{2}\left(\frac{L}{h}\right)^2$$

with the velocity of

$$\frac{u}{V_m}=-6\frac{x}{h}\frac{y}{h}\left(\frac{y}{h}-1\right)$$

and

$$\frac{V}{V_m}=2\left(\frac{y}{h}\right)^3-3\left(\frac{y}{h}\right)^2$$

As $\xi\rightarrow 0$ we have

$$u=\frac{p_x}{\eta}\left(y^2-H^2\right)+\frac{\varepsilon p_x^3\lambda^2}{\eta^3}\left(y^4-H^4\right)$$

For a 3D problem this model studies a flow of Oldroyd-B fluid past a cylinder between two parallel plates. The flow is considered as being two-dimensional (2D). The aspect ratio of the cylinder radius to the channel half-width is 1/2. To avoid the entrance and exit effects, the computational domain is 40 times longer than the channel half-width. The fluid is a dilute solution of polymer in a Newtonian liquid solvent of viscosity ηs. The total stress is presented as:

$$\begin{bmatrix}\sigma_x & \tau_{xy}\\ \tau_{xy} & \sigma_y\end{bmatrix}=\begin{bmatrix}-p & 0\\ 0 & -p\end{bmatrix}$$

$$+2\mu_s\begin{bmatrix}e_x & e_{xy}\\ e_{xy} & e_y\end{bmatrix}+\begin{bmatrix}T_x & T_{xy}\\ T_{xy} & T_y\end{bmatrix}$$

$$\begin{bmatrix}\sigma_x & \tau_{xy} & \tau_{xz}\\ \tau_{xy} & \sigma_y & \tau_{yz}\\ \tau_{xz} & \tau_{yz} & \sigma_z\end{bmatrix}=\begin{bmatrix}-p & 0 & 0\\ 0 & -p & 0\\ 0 & 0 & -p\end{bmatrix}$$

$$+2\mu_s\begin{bmatrix}e_x & e_{xy} & e_{xz}\\ e_{xy} & e_y & e_{yz}\\ e_{xz} & e_{yz} & e_z\end{bmatrix}+\begin{bmatrix}T_x & T_{xy} & T_{xz}\\ T_{xy} & T_y & T_{yz}\\ T_{xz} & T_{yz} & T_z\end{bmatrix}$$

where u = (u, v) is the flow velocity vector, p is the pressure In code

So we should change $\rho\equiv \mathrm{Re},\ \ \mu\equiv\mu_s$ to solve

$$\mathrm{Re}(u.\nabla)u=\nabla.(-pI+\mu_s\left[\nabla u+(\nabla u)^T\right]+T)$$

Also the general form PDE for the solution of

$$\frac{\partial}{\partial t}\begin{bmatrix} T_x & T_{xy} \\ T_{xy} & T_y \end{bmatrix} =$$
$$-Wi\left((u.\nabla)T + \left[(\nabla u)T + T(\nabla u)^T\right]\right)$$
$$+\mu_p\left[(\nabla u) + (\nabla u)^T\right]$$

Where is for each component

$$u.\nabla = u\frac{\partial}{\partial x} + v\frac{\partial}{\partial y}$$

The extra stress contribution due to the polymer is given by the following Oldroyd-B constitutive relation:

$$T + \lambda\frac{\Delta T}{\Delta t} = 2\eta_p e(u)$$

where the upper convective derivative operator (or Oldroyd derivative) is defined as

$$\frac{\Delta T}{\Delta t} = \frac{\partial T}{\partial t} + (u.\nabla)T - \left[(\nabla u)T + T(\nabla u)^T\right]$$

The polymer is characterized by two physical parameters: The viscosity ηp and the relaxation time λ. The fluid is treated as incompressible with a constant density ρ; the flow equations read:

$$\rho\frac{\partial u}{\partial t} + \rho(u.\nabla)u = \nabla.\sigma$$
$$\nabla.\sigma = 0$$

The extra stress tensor is symmetric:

$$T = \begin{bmatrix} T_{11} & T_{12} \\ T_{121} & T_{22} \end{bmatrix}$$

Therefore, it is necessary to solve three additional equations, for the three components in Equation 3, together with three equations given by Equation 5 for the pressure and two velocity components.

The Weissenberg number is defined as:

$$Wi = \lambda\frac{U_{in}}{R}$$

where Uin is the average fluid velocity at the inlet, R is the radius of the cylinder, and λ is the polymer relaxation time. (An alternative name, which is often used for this nondimensional parameter, is the Deborah number.) A zero Weissenberg number gives a pure viscous fluid (no elasticity) while an infinite Weissenberg number limit corresponds to purely elastic response. Due to the convective nature of the constitutive relation, the solution stability is lost with the increasing fluid elasticity. In practice, already the values Wi > 1 are considered as a high Weissenberg number for many flows of an Oldroyd-B fluid. By adding least squares-type stabilization terms to the Galerkin finite element formulation, you can improve stability and obtain solutions over a larger range of Weissenberg numbers compared to standard Galerkin formulations. The present model makes use of such least-squares stabilization technique. The flow is stationary, and the problem becomes dimensionless by using R, Uin, and the total viscosity η = ηs + ηp. The nondimensional equations system is the following:

$$\mathrm{Re}(u.\nabla)u = \nabla.(-pI + \mu_s\left[\nabla u + (\nabla u)^T\right] + T)$$

$$T + Wi\left((u.\nabla)T - \left[(\nabla u)T + T(\nabla u)^T\right]\right)$$
$$= \mu_p\left[(\nabla u) + (\nabla u)^T\right]$$

where the Reynolds number is Re = R Uinη / ρ, and the relative viscosities of the solvent and polymer are, respectively: μs = ηs / η and

$$\mu_p = \frac{\eta_p}{\eta} = 1 - \mu_s$$

Weak formulation of the above equations and the stabilization terms needed for the extra stress equations are not shown here. For details, see Ref. 1.

Because of the flow symmetry, you model only the upper halves of the channel the cylinder. At the channel centerline, use the symmetry conditions of zero normal flow and zero total tangential stress:

$$u.n = 0$$
$$(\sigma.n).t = 0$$

where **n** and **t** are the boundary unit normal and tangent vectors, respectively. On a horizontal line of symmetry, the latter condition is reduced to

$$2\mu_s e_{12} + T_{12} = 0$$

At the channel walls and the cylinder surface, the model uses no slip conditions for the velocity together with the condition for the normal component of the extra stress:

$$(T.n).n = 0$$

Polymers are unable to exert a normal force on the wall because no polymer can span the wall boundary. *Half-Inlet* Here you specify the developed parabolic velocity profile and the corresponding extra stresses components:

$$u = \frac{3}{2}(1 - s^2)$$
$$T_{11} = 2\mu_p Wi\left(\frac{\partial u}{\partial y}\right)^2$$
$$T_{12} = \mu_p\left(\frac{\partial u}{\partial y}\right)$$
$$T_{22} = 0$$

where the geometry edge parameter *s* varies from 0 to 1 along the half-inlet boundary. *Outlet* At the outlet, use the pressure boundary condition for developed flow; the only stress acting at the boundary is due to the pressure force p_{out}:

$$\sigma.n = -p_{out}n$$

The continuum problem is discretized with the finite-volume method, where the governing equations translate to balances of the fluxes between discrete control volumes. The fluxes are evaluated by a *quadratic upwind interpolation* scheme with flux limiters (CUBISTA) introduced [15]. The equations are integrated in time with the *two-level backward differentiation formula* (BDF2). Our implementation of the VOF method uses the second-order accurate algorithm of Pilliod and Puckett [16], where the piecewise linear approximations of the interface are

reconstructed with the ELVIRA technique, and the advection is solved explicitly by an operator split algorithm. Because of the non-linearity, the volume fraction, constitutive and conservation equations are solved sequentially, with successive *direct substitution* iterations until a convergence criterion is reached, at each time-step.

The log-conformation reformulation of the constitutive equation was recently introduced by Fattal and Kupferman [8,9]. It expresses the viscoelastic extra-stress $\boldsymbol{\sigma}$ in the constitutive equation (4) in terms of the logarithmic conformation $\boldsymbol{s} = \log(\boldsymbol{c})$. The conformation tensor, defined as

$$\boldsymbol{c} = (\lambda/\mu_{\mathrm{p}})\boldsymbol{\sigma} + \boldsymbol{I},$$

is a measure of the extra-stress which has the important property of being *symmetric positive definite*, thus it has a real matrix-logarithm. The matrix-logarithm transformation requires the diagonalization of the conformation tensor, $\boldsymbol{c} = \boldsymbol{Q}\boldsymbol{D}\boldsymbol{Q}^{\mathrm{T}}$, where $\boldsymbol{D}$ is the diagonal matrix of the eigenvalues and $\boldsymbol{Q}$ is the orthogonal matrix containing the eigenvector as vector column. The matrix-logarithm is interpreted as

$$\log(\boldsymbol{c}) = \boldsymbol{Q}\log(\boldsymbol{D})\boldsymbol{Q}^{\mathrm{T}},$$

where the logarithm $\log(\boldsymbol{D})$ is applied component-wise. The evolution equation of the log-conformation is:

$$\frac{\partial \boldsymbol{s}}{\partial t} + \boldsymbol{u}\cdot\nabla\boldsymbol{s} - (\boldsymbol{\Omega}\boldsymbol{s} - \boldsymbol{s}\boldsymbol{\Omega}) - 2\boldsymbol{B} = \frac{f(e^{s})}{\lambda}e^{-s},$$

where the $\boldsymbol{\Omega}$ and $\boldsymbol{B}$ are pure rotation and pure extension decompositions of the velocity gradient $\nabla\boldsymbol{u}$. Finally, the divergence of the viscoelastic extra-stress is recovered though the matrix-exponential of $\boldsymbol{s}$. This change of variable ensures by construction the positive definiteness of the conformation tensor. Fattal and Kupferman also showed that the numerical instabilities at high Weissenberg numbers are due to poor resolution of the exponential stress growth in time, and the exponential stress profile near geometrical singularities [17], with quadratic approximations. In the log-conformation representation, such exponential growths/profiles become linear and are accurately approximated by linear and quadratic schemes.

The main difficulty when solving the conservation equations (2)-(3) with the velocity and pressure as primary unknowns ($\boldsymbol{u}$-p formulation), comes from the fact that there is no evolution equation for the pressure unknowns. Indeed, the pressure acts as a Lagrange multiplier of the incompressibility constraint which means that errors in the pressure fields directly link to errors in the conservation of mass. Most (if not all) viscoelastic algorithms use velocity-pressure fractional-step decoupling techniques, such as the SIMPLE, PISO or Chorin's projection methods [18-20]. The decoupling is achieved via an approximation of the inverse of the Jacobian matrix in the system of momentum equations. This approximation introduces a decoupling error; e.g. for the standard first order fractional-step method, the dominant error terms are proportional to $\Delta t/Re$ [21]. It means the decoupling technique is accurate at high *Re*, i.e. in flows driven by gravity or inertia, such as in aero-dynamics or hydro-dynamics problems. However, at low *Re* (especially below unity), the decoupling errors becomes very large. These flows are generally driven by pressure gradients, so that the velocity and pressure fields are strongly coupled. As a result, the decoupling techniques may not be the most suitable.

Alternatives to the $\boldsymbol{u}$-p formulation solve the momentum equation in its rotational form, where a transport equation for the vorticity $\boldsymbol{\omega} = \nabla\times\boldsymbol{u}$ is derived [22], e.g. the $\boldsymbol{u}$-$\boldsymbol{\omega}$ formulation and the $\boldsymbol{\psi}$-$\boldsymbol{\omega}$ formulation. As a result, the pressure unknowns are eliminated from the system of equations. Here we use a more robust formulation, the *pure-streamfunction formulation*, recently introduced by Kupferman [10] and by Chang, Giraldo and Perot [11], independently. It also uses the rotational form of the momentum equation, but all the kinematic unknowns are expressed in terms of a streamfunction $\boldsymbol{\psi}$, defined as a vector potential of the velocity field:

$$\boldsymbol{u} = \nabla\times\boldsymbol{\psi},$$

and linked to the vorticity by a Poisson equation:

$$\boldsymbol{\omega} = \Delta\boldsymbol{\psi}.$$

The advantage of the pure-streamfunction formulation is that the continuity constraint is automatically fulfilled, by construction. In the 2D case, only one component of $\boldsymbol{\psi}$ is non-zero: $\boldsymbol{\psi} = (0,0,\psi)$, therefore the streamfunction vector reduces to a scalar field φ, where

$$(u,v) = \nabla^{\perp}\boldsymbol{\psi} = \left(-\frac{\partial\psi}{\partial y}, \frac{\partial\psi}{\partial x}\right). \tag{1}$$

Then, the evolution equation for the streamfunction scalar reads:

$$\frac{\partial}{\partial t}\Delta\psi + \left[\left(\nabla^{\perp}\psi\right)\cdot\nabla\right]\Delta\psi = \frac{\mu_S}{\rho}\Delta^2\psi + \nabla\times\left(\nabla\cdot\boldsymbol{\sigma}\right), \tag{2}$$

In general, this formulation is more robust and accurate as it is fully implicit and does not produce errors. For details about the discretization procedure of the 4th order operators, see in reference [11].

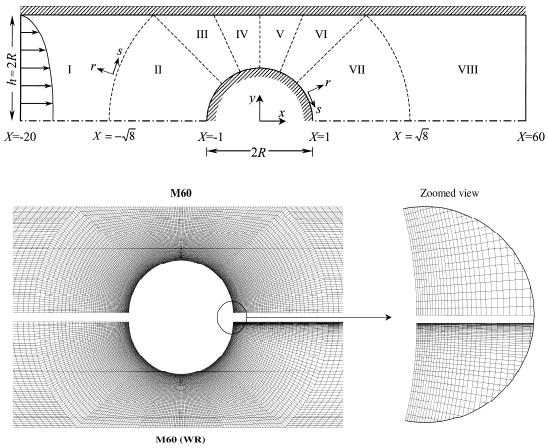

Figure 2. Mesh regions

RESULTS AND DISCUSSION

For the exponential form of the PTT fluid, the results of our calculations for ε=0.25 are depicted in Fig. 3-7, giving XR versus De; in Fig. 8-12, giving ΨR versus De; and in Fig. 13-15, versus De; the corresponding numerical data. Again, fair agreement is seen with computations by Aboubacar et al. [8], except at De=0.1 for the reasons noted above. However, except for two values of the recirculation intensity at De=100 and 1000, the uncertainty is generally below 1%. In these runs, it was important to use an extended length for the downstream channel as De was increased, according to the estimate given by Eq. (11); otherwise, the discrepancy between results on meshes M2 and M4 would be visible in the figures. M4 was deemed adequate for this fluid case; runs at De=1 and 100 on meshes M4 and M6 showed a difference in XR below 0.1 and 0.5% for ΨR.

Current solution method for 2D viscoelastic flow was implemented in Matlab. We first test our algorithm for the simulation of Newtonian and viscoelastic flows at very low *Re* in the 4:1 contraction geometry, without free-surfaces. The geometry is discretised using a uniform orthogonal mesh, with 40 control volumes on the width of the downstream channel. The no-slip boundary condition is applied at the walls, and the fully-developed velocity and stress profiles are imposed at the inlet. We use an Oldroyd-B material with a viscosity ratio $\beta = \mu_S / (\mu_S + \mu_P) = 1/9$. The fluid is initially at rest, and after a short transient response the flow establishes a steady-state solution. In our calculation, the steady-state solution was found stable for $Wi < 4$, while a hydrodynamic instability developed from $Wi = 4$ and above. This instability is not a numerical instability since the simulation does not diverge. The streamlines are perturbed inside the downstream channel. Oscillations of the velocity in the spanwise direction

partially separate the stress boundary-layers from the walls, as depicted in the figure 1. The flow perturbation was initiated near to the re-entrant corner and later propagated inside downstream. It is interesting to note that the perturbation started where the streamlines have high curvatures and the material experiences the largest shear deformation. This is an indication that this flow instability could correspond to a (physical) elastic instability [5].

The analysis gradually increases the Weissenberg number from 0 to 1 using the parametric solver. Figure 1 and Figure 2 show the flow field and stress distribution for a typical value of Wi = 0.7. Figure 3 shows the drag coefficient as a function of the Weissenberg number. The result is in good agreement with the experimental and simulation results presented in Ref. 2. In order to validate the code, we compare our results with the experimental data of Bara et al. [6] in Fig. 3, where velocity profiles extracted from the middle plane of the duct (Z = 0.5) at different positions along the curve are presented. The solid lines represent our results and the symbols pertain to the data of Bara et al. [6] for three values of the Reynolds numbers (Re = 486, 532 and 583). Good agreement was obtained for all cases thus validating the numerical method and confirming again the adequateness of the mesh resolution.

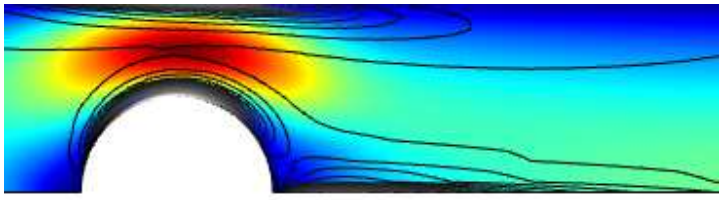

Figure 3. Flow field near cylinder and stress distribution for Wi = 0.7

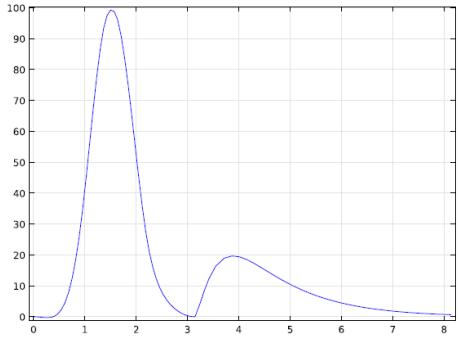

Figure 4. Stress distribution along the cylinder surface and wake centerline for Wi = 0.7

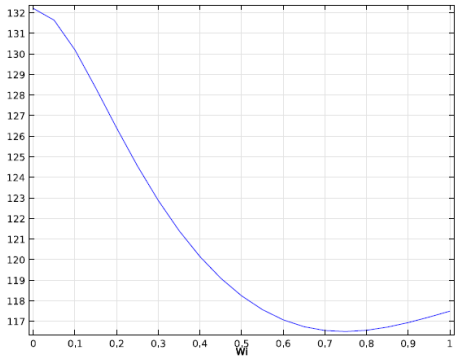

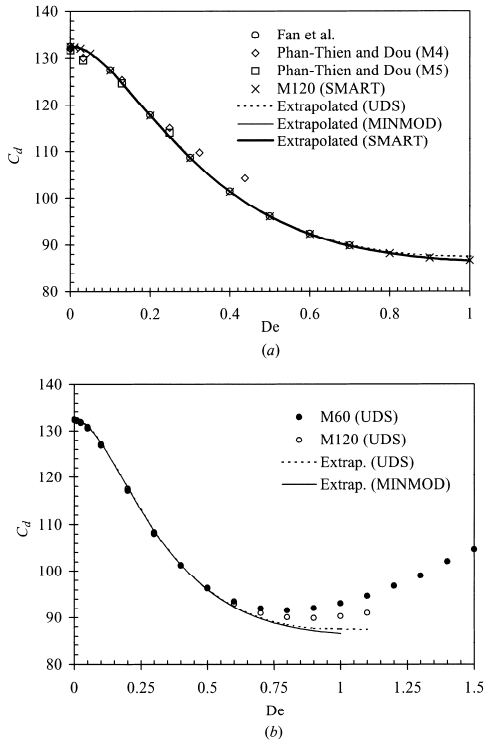

Figure 5. Drag on the cylinder

In Fig. 7 the streamlines for the Oldroyd-B fluid, computed on the finest mesh M6, are presented. These show, qualitatively, shrinkage of the corner vortex with raising elasticity and the appearance of a small lip vortex at around De≈1. Although minute, the lip vortex is not an artifact of the computations: it is shown in Fig. 8 that its intensity is finite with extrapolation to a zero mesh size (recall that our mesh is very refined in the region around the re-entrant corner). From Fig. 8 it is also clear that, while for De=0.5 and 1 the lip vortex vanishes when the grid resolution is infinitely increased, for De=1.5 a finite lip vortex intensity remains when $\Delta x \rightarrow 0$. Such behaviour is more clearly shown in Fig. 9, where lip vortex streamlines are plotted over an enlarged local view of the various meshes, and in Fig. 6 where the asymptotic variation of lip vortex size and intensity with mesh fineness indicates finite values for zero mesh size. Note the linear convergence of the lip vortex characteristics, in contrast to the general quadratic convergence rate of the scheme; this is the best it can be achieved with such a small and localised flow feature as the lip vortex. Similar, but stronger, lip vortices were present in our previous simulations with the upper convected Maxwell model [6] and [12].

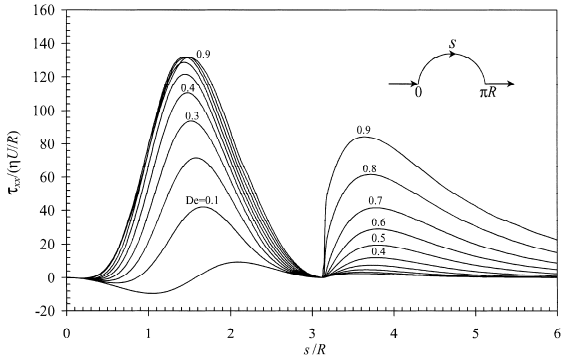

Figure 6. Profiles of longitudinal normal stress along cylinder wall and wake centreline for UCM fluid at increasing De

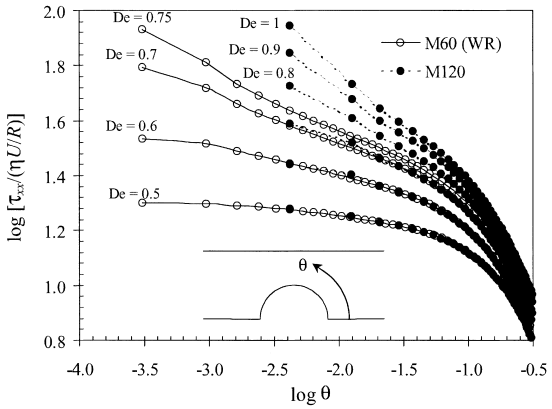

Figure 7. Asymptotic behaviour of the normal stress with the azimuthal position for increased elasticity

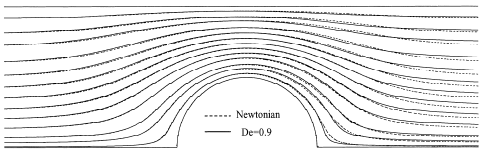

Figure 8. Zoomed view of the streamlines for a Newtonian fluid (dashed line) and an Oldroyd-B fluid at De= 0.9

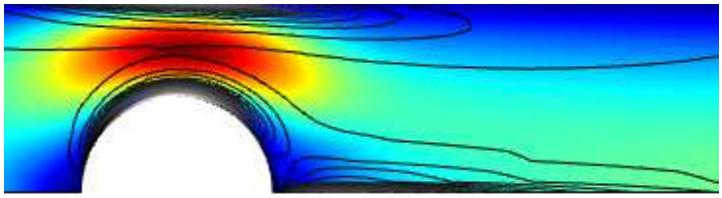

Figure 9. Streamlines and velocity magnitude for PTT fluid at De= 1

A view of the various stress component fields (τxx, τyy, τxy) and the pressure field in the entrance region is provided in Fig. 10. These predictions were obtained on the finest mesh M6 and correspond to the highest Deborah number achieved, De=2.5. All fields are smooth, with highly localised stress concentration at the walls adjacent to the re-entrant corner. A more quantitative view of the local velocity and stress variations can be gained from asymptotic type of plots, which also serve to check some of the existing theories. These kinds of plots show radial profiles under log–log scales, emanating from re-entrant corner (distance r), at given angles θ measured anticlockwise from the incoming flow direction (see Fig. 2). The most convenient angle is θ=90° which corresponds to profiles across the flow, along the Cartesian co-ordinate y, at x=0; Fig. 11 shows such profiles on various meshes for the Oldroyd-B fluid at De=1. This value of De was chosen to avoid the formation of a lip vortex which would violate the assumptions of the asymptotic theories (e.g. [19]). The predictions shown in Fig. 11 reveal good convergence when the computational meshes are refined, with the longitudinal and transversal velocity components going to zero near the corner as $r^{5/9}$ and $r^{3/4}$, respectively, and all three stress components going to infinity as $r^{-2/3}$; these slopes agree with the theory of Hinch [19]. Further study of the asymptotic behaviour of the UCM fluid (which essentially follows the Oldroyd-B behaviour) was given in a previous work [20], where both the Deborah number and the angle of the radial line were varied.

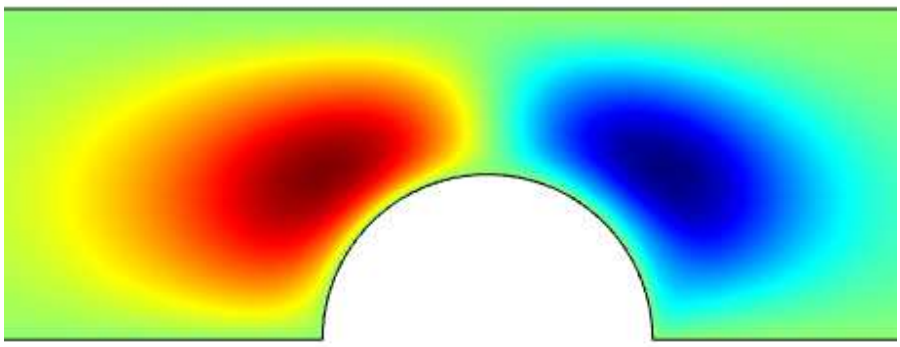

Figure 10. Vertical velocity contour for PTT fluid at De= 1

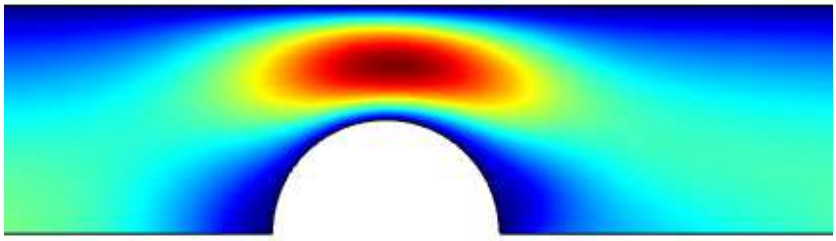

Figure 11. Horizontal velocity for PTT fluid at De= 1

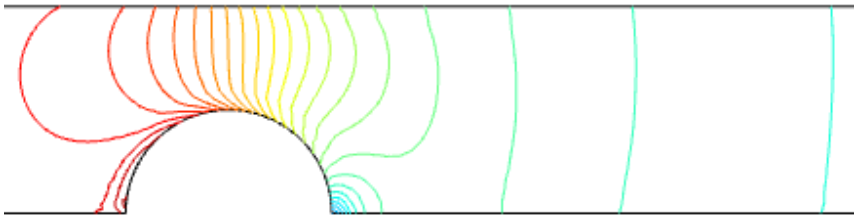

Figure 12. Pressure contour for PTT fluid at De= 1

This model is shear thinning on both the shear viscosity and the first normal stress difference coefficient. In addition, the elongational viscosity is limited; reaching a plateau at high strain rates, and the maximum value of the elongational viscosity varies inversely with the parameter ε. The first set of results to be presented corresponds to ε=0.25, a typical value for the flow of concentrated polymer solutions and/or also for polymer melt flows. Contrary to the Oldroyd-B fluid, both the size and intensity of the corner vortex for the linear PTT fluid are seen in Fig. 13 and Fig. 14 to increase monotonically with the Deborah number. Also, there is less sensitivity to mesh fineness, except possibly at high De, but not as noticeable as for the Oldroyd-B fluid. For purposes of benchmarking, all our results are tabulated in Table 3 with quantified uncertainties. For comparison, the data of Aboubacar et al. [8] are plotted in these figures; there is fair agreement, except for some erratic points. Notice also that the vortex recirculation tends to level out at high elasticity and so the linear PTT model is not able to predict the very large corner vortices observed in some experimental visualisation works (see [21] and references therein).

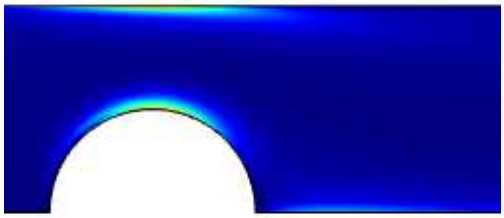

Figure 13. T_{11} for PTT fluid at De= 1

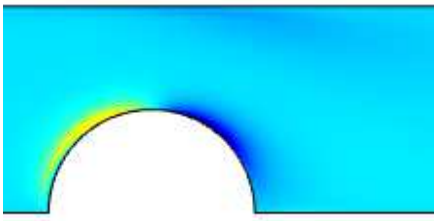

Figure 14. T_{12} for PTT fluid at De= 1

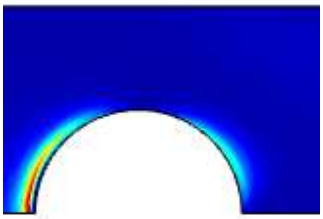

Figure 15. T_{22} for PTT fluid at De= 1

CONCLUSION

Accurate predictions for the flow around a confined cylinder (blockage ratio 0.5) are obtained with a general collocated FVM incorporating two high-resolution schemes to represent the convective terms in the constitutive equation. A consistent mesh refinement study and the application of Richardson's extrapolation to the solution functional Cd allowed us to determine the apparent (or observed) order of convergence of the schemes. These estimates are valid De< 0.9 in which we achieve the asymptotic range for the four finer meshes. The present Cd results can be used as benchmark data with an estimated accuracy in the finer mesh of 0.03% for the UCM and 0.01% for the Oldroyd-B fluids (except for the last available De, for which we obtain 0.07% for UCM at De D 0:9, and 0.03% for Oldroyd-B at De D 1). For this problem, which is usually classified under the category of "smooth flow", we have consistent predictions of Cd up to De < 0.7 between the present FVM and the FEM of Fan et al. [9] who used an highly accurate h-p refinement technique with polynomials of degree up to 6. Other FEM and CVFEM results from the literature start deviating from the present Cd data, and that of [9], at De ├ 0:3 (UCM) and De <0.4 (Oldroyd-B), typically exhibiting higher Cd values, an indication of loss of accuracy. It is thus, established that FVM can yield accurate results, provided the discretisation of the constitutive equation and the level of mesh refinement are adequate, in line with opinions vehiculated by Dou and Phan-Thien [11] and Baaijens [36] regarding the need to use higher-order schemes in FVM. In fact, if anything the present decoupled FVM proved to be more robust than the coupled FEM of [9] with solutions for the UCM model up to De <1:0 using MINMOD. However, findings of Fan et al. [9] related to difficulties to attain mesh converged results in the wake of the cylinder at high Deborah numbers are confirmed. In a wake-refined mesh, the maximum normal stresses in the wake are seen to increase as De3 and as De5 for low and high Deborah numbers, respectively.

Acknowledgements
The MYAJ would like to acknowledge the rheology course lecturer, Prof. Vlasis Mavrantzas; and also great appreciation to Prof. John Tsamopoulos for his novel ideas, patient and supports.

REFERENCES

[1] MY Abdollahzadeh Jamalabadi, *J Porous Media*, **2015**, 18(9) ,843-860.
[2] MY Abdollahzadeh Jamalabadi; JH Park, *Therm Sci*, **2014**, 94-94
[3] MY Abdollahzadeh Jamalabadi, *Int J Opt Appl*, **2015**, 5 (5) , 161-167
[4] MY Abdollahzadeh Jamalabadi, *Chem Eng Res Des*, **2015**, 102 , 407-415
[5] MY Abdollahzadeh Jamalabadi ; JH Park, *World App Sci Journal* , **2014**, (4)32 , 672-677
[6] MY Abdollahzadeh Jamalabadi; JH Park ; CY Lee, *entropy*, **2015**, 17 (2), 866-881
[7] A Shahidian; M Ghassemi; S Khorasanizade; M Abdollahzade; G Ahmadi, *IEEE Trans Magn*, **2009**, 45 (6)2667-2670
[8] MY Abdollahzadeh Jamalabadi, *J. Marine Sci & App*, **2014**, 13 (3) 281-290
[9] MY Abdollahzadeh Jamalabadi ; JH Park, *Int J. Sci Basic App Res Sci 1* , **2014**, 421-427
[10] MY Abdollahzadeh Jamalabadi ; JH Park, *Open J. Fluid Dyn*, **2014**, 23 (4) 125-132
[11] MY Abdollahzadeh Jamalabadi;JH Park;MM Rashidi ;JM Chen, *J. Hydrod Ser. B*, **2016**
[12] MY Abdollahzadeh Jamalabadi, *Front Heat Mass Trans*, **2015**, 6,013007
[13] M.Y. Abdollahzadeh Jamalabadi, *J. Fuel Cell Sci. Technol*, **2013**, 10(5) , 1039
[14] MY Abdollahzadeh Jamalabadi;JH Park; CY Lee, *Therm Sci*, **2014**, 124-124
[15] M Jamalabadi; P Hooshmand; B Khezri ; A Radmanesh, *Ind J sci Res* 2 , **2014**, 74-81
[16] MY Abdollahzadeh Jamalabadi, *Mul Model Mat Struc* , **2016**
[17] M.Y. Abdollahzadeh Jamalabadi, J.H.Park,C.Y. Lee, *International Journal of Applied Environmental Sciences*, **2014**, 9 (4) 1769-1781
[18] MY Abdollahzadeh Jamalabadi, *World App. Sci. J.* **2014**, 32 (4) 667-671
[19] MY Abdollahzadeh Jamalabadi, *Mid-East J. Sci Res* **2014**, 22 (4) 561-574
[20] MY Abdollahzadeh Jamalabadi, *Mat . Perf. Char*, **2015** 20140062
[21] MS Shadloo;R Poultangari; MY Abdollahzadeh Jamalabadi, MM Rashidi , *Energy Conversion and Management*, **2015**,96 , 418-429
[22] MY Abdollahzadeh Jamalabadi; M Ghasemi; MH Hamedi , *Int J Numer Meth Heat Fluid Flow*, **2013**, 23 (4) 649-661
[23] MY Abdollahzadeh Jamalabadi, *Int J Ener Mat Chem Pro*, **2016** 15,
DOI: 10.1615/IntJEnergeticMaterialsChemProp.2015014428
[24] MY Abdollahzadeh Jamalabadi, *Noise and Vibration Worldwide*, **2014**, 45 (8) 21-27
[25] MY Abdollahzadeh Jamalabadi, *J. King Saud Univ Eng Sci*, **2014**, 26 (2) 159-167
[26] MY Abdollahzadeh Jamalabadi ; M Ghasemi ;MH Hamedi, *Proc Inst Mech Eng, Part C, J. Mech Eng Sci*, **2012** ,(226) 1302-1308
[27] M.Y. Abdollahzadeh Jamalabadi, *Int J Ener Eng*, **2015**, 5(1) 1-8
[28] M.Y. Abdollahzadeh Jamalabadi, *Int J Mult Res Dev*, **2014**, (1) 5 ,1-4
[29] S Dousti; J Cao; A Younan; P Allaire; T Dimond, *J. tribology* , **2012**,134 (3), 031704.
[30] S Dousti; JA Kaplan, F He; PE Allaire, *ASME Turb Exp Conf* , **2013**.
[31] F He; PE Allaire; S Dousti; A Untaroiu , *ASME Int Mech Eng Cong Exp*, **2013**.
[32] S Dousti; RL Fittro, *ASME Turb Exp Conf* , **2015**.
[33] E Sarshari; N Vasegh;M. Khaghani; S Dousti, ASME Int Mech Eng Cong Exp, **2013**.
[34] S Dousti; TW Dimond; PE Allaire, HE Wood, ASME Int Mech Eng Cong Exp, **2013**.
[35] S Dousti;MA Jalali, *J. App Mech*, **2013**, 80 (1), 011019.
[36] S Bita; MY Abdollahzadeh Jamalabadi, MY; M Mesbah, *J. Chem. Pharm. Res*., **2015**, 7(11):91-98
[37] MY Abdollahzadeh Jamalabadi, *Int J of Eng and App Sci*, **2015** , 7 (5)
[38] MY Abdollahzadeh Jamalabadi; M Dousti; H Jafarzadeh; F Dadgostari, *Int. J Eng & Adv Tech*, **2015**, 5 (2): 118-124
[39] MY Abdollahzadeh Jamalabadi , *J of Nig Math Soc*, **2016**
[40] MY Abdollahzadeh Jamalabadi; S Dousti; *J. Chem. Pharm. Res*., **2015**, 7(12)
[41] MS Shadloo; R Weiss; M Yildiz; RA Dalrymple, *Int J Offshore Polar*, **2015**, 25 (1), 17.
[42] F Mabood; SM Ibrahim; MM Rashidi; MS Shadloo, G Lorenzini, *Int J Heat Mass Tran*, **2016** (93) 674-682.
[43] MS Shadloo; A Hadjadj; F Hussain, *Int J Heat Fluid Fl*, **2015** (53) 113-134.

[44] MS Shadloo; R Poultangari; MYA Jamalabadi; MM Rashidi, *Energ Convers Manage*, **2015** (96) 418- 429.
[45] A Hadjadj; O Ben-Nasr; A Chaudhuri; MS Shadloo, *Int J Heat Mass Tran*, **2015** (81) 426438.
[46] MS Shadloo; A Hadjadj; A Chaudhuri, *Phys. Fluids*, **2014** (26) 076101.
[47] A Rahmat; N Tofighi; MS Shadloo; M Yildiz, *Colloids and Surfaces* A, **2014** (460) 60-70.
[48] R Fatehi; MS Shadloo; MT Manzari, *P I Mech Eng C-J Mec*, **2014** (228) 1913- 1924.
[49] MS Shadloo; A Rahmat; M Yildiz, *Comput Mech*, **2013** (52) 693-707.
[50] MS Shadloo; A Kimiaeifar; D Bagheri, *Int J Numer Method H Fl F*, **2013** (23) 289-304.
[51] A Zainali; N Tofighi; MSShadloo; M Yildiz, *Comput. Methods in Appl. Mech. Eng*., **2013** (254) 99-113.
[52] MS Shadloo; A Zainali; M Yildiz, *Comput Mech*, **2013** (51) 699-715.
[53] MS Shadloo; A Zainali; M Yildiz; A Suleman, *Int J Numer Meth Eng*, **2012** (89) 939- 956.
[54] MS Shadloo; M Yildiz, *Int J Numer Meth Eng*, **2011** (87) 988-1006.
[55] MS Shadloo; A Zainali; SH Sadek; M Yildiz, *Comput. Methods in Appl.Mech.Eng*., **2011** (200) 1008− 1020.
[56] MS Shadloo; A Kimiaeifar, P I *Mech Eng C-J Mec*, **2011**, 225(2), 347-353.
[57] MS Shadloo; A Zainali; M Yildiz, FEDSM-ICNMM 2010-31135, 1-4 Aug. **2010**, Montreal, Québec, Canada.
[58] MS Shadloo; A Zainali; M Yildiz, FEDSM-ICNMM 2010-31137, 1-4 Aug. **2010**, Montreal, Québec, Canada.
[59] MS Shadloo; D Le Touze; G Oger, Manuscript No.: 2015-TPC-0750, 25th IOPE Conf., June 21-26, **2015**, Kona, Big Island, Hawaii, USA.
[60] H Akherat Doost; MS Shadloo; M Salehi, Sharif J Sci. Tech., **2011**, reference number: 40/358/89930.
[61] AG Kaviri Nejad; MS Shadloo; A Kimiaeifar, M Ghasempour, *Aust. J. Basic appl. sci*. **2010**, 4(9): 4205-4212.
[62] R Poultangari; MS Shadloo, *J Conv. Energy*, **2010**, 1(1) 49-61.
[63] MS Shadloo; M Yildiz, 7th ICNAAM, 19-25 Sept., **2012**, Kos, Greece.